Bull. Mater. Sci., Vol. 39, No. 7, December 2016, pp. 1765–1774. © Indian Academy of Sciences.
DOI 10.1007/s12034-016-1305-9

# Structural, optical spectroscopy, optical conductivity and dielectric properties of $BaTi_{0.5}(Fe_{0.33}W_{0.17})O_3$ perovskite ceramic

**FAYÇAL BOURGUIBA[1,*], AHMED DHAHRI[2], TAREK TAHRI[2], KAMEL TAIBI[3], JEMAI DHAHRI[1] and E K HLIL[4]**

[1]Laboratory of Condensed Matter and Nanosciences, Faculty of Sciences of Monastir, Monastir 5019, Tunisia
[2]Laboratoire de Physique Appliqué, Département de Physique, Faculté des Sciences de Sfax, 3018 Sfax, Tunisia
[3]Laboratoire de Science et Génie des Matériaux, Faculté de Génie Mécanique et Génie des Procédés, Université des Sciences et de la Technologie Houari Boumediene, BP32 El Alia, Bab Ezzouar 16111, Algeria
[4]Institut Néel, CNRS-Université J. Fourier, B.P. 166, 38042 Grenoble, France

MS received 31 January 2016; accepted 15 April 2016

**Abstract.** **Fe and W co-substituted $BaTiO_3$ perovskite ceramics, compositional formula $BaTi_{0.5}(Fe_{0.33}W_{0.17})O_3$, were synthesized by the standard solid-state reaction method and studied by X-ray diffraction, scanning electron microscopy and spectroscopy ellipsometry. The prepared sample remains as double phases with the perovskite structure. The structure refinement of $BaTi_{0.5}(Fe_{0.33}W_{0.17})O_3$ sample was performed in the cubic double and hexagonal setting of the $Fm\bar{3}m$ and $P6_3/mmc$ space groups. Spectral dependence of optical parameters; real and imaginary parts of the dielectric function, refractive index, extinction coefficient and absorption coefficient were carried out in the range between 1.4 and 4.96 eV by using the ellipsometry experiments. Direct bandgap energy of 4.36 eV was found from the analysis of absorption coefficient *vs.* photon energy. In addition, the oscillator energy, dispersion energy and zero-frequency refractive index values were found from the analysis of the experimental data using Wemple–DiDomenico single-effective-oscillator model.**

**Keywords.** **Perovskite; $BaTiO_3$; X-ray diffraction; spectroscopic ellipsometry; refractive index.**

## 1. Introduction

Ferroelectric oxides with perovskite structure are the subject of many investigations. As ferroelectric materials, barium titanate $BaTiO_3$ (BT) and BT-based materials are the most studied perovskite systems and are being considered as a potential candidate in ceramic and electronic industries [1]. This is because of the fact that it possesses a high dielectric permittivity at room temperature, large piezoelectric and pyroelectric coefficients, comparable with lead-based perovskite ferroelectrics, does not contain toxic elements and is characterized by relatively low production costs. Barium titanate has been broadly used as a dielectric material in multilayer ceramic capacitors [2], printed circuit boards [3], dynamic random access memory, positive temperature coefficient of resistance thermistors, piezoelectric sensors for ultrasonic and measuring devices, pressure transducers, infrared detectors and electrooptic devices [4–6].

$BaTiO_3$, which is a typical $ABO_3$ perovskite-type material, has five kinds of crystal systems: hexagonal, cubic, tetragonal, orthorhombic and rhombohedral, depending on the phase transition temperatures: 1432, 130, 5 and −90°C. The tetragonal phase is the most stable phase at room temperature [7]. These characteristics depend, also, on the type of substitutions, isovalent or heterovalent [8] ions, and their location in the crystal sub-lattice for Ba-site and/or Ti-site. It is known from the literature [9–14] that in case of the B-site substitution, substantial replacement of $Ti^{4+}$ by $Fe^{3+}$ and/or $W^{6+}$ affects the structure and physical properties. The substitution of iron in Ref. [14] helps to stabilize the structure in the hexagonal phase at room temperature and leads to an energy gap of 3.4 eV. The substitution of tungsten has been found to be effective in enhancing the dielectric properties of ferroelectric materials [9,10]. The X-ray diffractograms in $Ba(Ti_{1-x}W_x)O_3$ [10] show the crystallization of these materials with tetragonal structure. Moreover, the dielectric constant as well as loss decreases with the increase of frequency. In $Ba_3Fe_2WO_3$ [12], the titanium is completely substituted by a different portion of iron and tungsten. In this case, the compound adopts the hexagonal 6H-perovskite structure with space group $P6_3/mmc$, which are the same in Refs [11,13,14]. However, there has not been much work on tungsten and iron substitution in the B-site of the barium titanate structure. This encouraged us to investigate the structural, morphological and optical properties (optical constants, optical bandgap, Urbach energy, dispersion parameters and dielectric functions) of $BaTi_{0.5}(Fe_{0.33}W_{0.17})O_3$. Thus, researchers can apply these materials in optical devices and heterojunction solar cells.

*Author for correspondence (faycel.bourguiba@gmail.com)

## 2. Experimental

In this article, $BaTi_{0.5}(Fe_{0.33}W_{0.17})O_3$ is denoted as BTFW. Polycrystalline sample with this nominal composition was prepared from high-purity (more than 99.9%) powders of $BaCO_3$, $TiO_2$, $Fe_2O_3$ and $WO_3$, using the conventional solid-state reaction method. The starting materials were intimately mixed in an agate mortar and calcined at 1173 K for 24 h and then at 1373 K for 2 days with an intermediate regrinding. After calcination, powders were mixed for 1 h and pressed under 4 T $cm^{-2}$ into 8 mm diameter and 1 mm thickness. Finally, the pellets were sintered at 1673 K in air for 4 h followed by furnace cooling. Phase purity, structure, space groups and lattice parameters were determined by powder X-ray diffraction (XRD) with a Siemens D5000 diffractmeter using Cu-K$\alpha$ radiation ($\lambda = 1.540598$ Å) at room temperature. Data for Rietveld refinement were collected in the range $10 \leq 2\,\theta \leq 100$ by step scanning of 0.0167° and counting time of 17 s per step. Refinements were carried out using FULLPROF program based on the Rietveld method [15]. Profile refinement parameters included a scale factor, pseudo-Voigt peak shape parameters, a peak full-width at half-maximum (FWHM) function of the form $(\mathrm{FWHM})^2 = U \times \tan(2\theta) + V \times \tan(\theta) + W$, a $2\theta$ zero parameter and unit cell parameters. The background was refined to a six-degree polynomial. The grain size and the micromorphology have been detected on a facture surface by a scanning electron microscope (SEM) using a Philips XL30 equipped with energy dispersive X-ray detector. The optical constants such as refractive index ($n$), extinction coefficient ($k$) and dielectric constants ($\varepsilon_1$, $\varepsilon_2$), were measured at room temperature at an incident angle 70° in the range 1.40–4.96 eV (250–880 nm) using an automatic ellipsometer SOPRA GE 5E. In the spectroscopic ellipsometry (SE), one deals with the measurements of the relative changes in the amplitude and the phase of linearly polarized monochromatic incident light upon oblique reflection from the sample surface [16].

## 3. Results and discussion

### 3.1 *Structural study*

XRD analysis was performed to establish the phases present in this compound. The powder XRD pattern of BTFW ceramic powder obtained by crushing the sample sintered at 1673 K for 4 h is shown in figure 1. This diffractogram shows that BTFW compound is a mixture of cubic double and hexagonal pervoskite phases with the space group $Fm\bar{3}m$ and $P6_3/mmc$, respectively. The cubic double and hexagonal structures can be distinguished by characteristic peaks at about $2\theta = 31°$. In this region of $2\theta$ angular position, we notice the existence of a split peak: one at a lower degree and the other at a higher degree, which represent the hexagonal structure and the cubic double structure, respectively (see the inset of figure 1). The relative amounts of cubic double and hexagonal phases were determined from XRD patterns of the

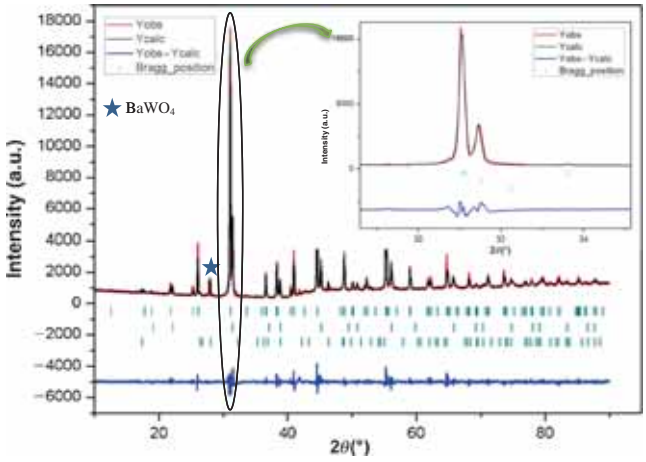


**Figure 1.** Rietveld plots of XRD data for polycrystalline $BaTi_{0.5}Fe_{0.33}W_{0,17}O_3$. The points are the observed profile; the solid lines are calculated value. Positions for the Bragg reflection are marked by vertical bras. The line curve at the bottom of the diagram gives the difference between observed and calculated profiles. Inset shows an enlarged view of peak ~32°.

sample by measuring the relative intensities of the (220) major cubic double peak $I_{\mathrm{cub}}$ and the (110) major hexagonal peak $I_{\mathrm{hex}}$ by the following quantitative equations [17]:

$$\text{Double cubic}(\%) = 100 \times \frac{I_{\mathrm{cub}}}{I_{\mathrm{cub}} + I_{\mathrm{hex}}}. \tag{1}$$

$$\text{Hexagonal}(\%) = 100 - \text{double cubic}(\%) = 100 \times \frac{I_{\mathrm{hex}}}{I_{\mathrm{cub}} + I_{\mathrm{hex}}}. \tag{2}$$

Table 1 shows the values of intensities and $2\theta$ corresponds to (220) cubic double peak and (110) hexagonal peak. The relative amount of the double cubic phase was 23.9; however, the relative amount of the hexagonal phase was 76.1%. Consequently, we can conclude that the relative amount of the hexagonal phase is the dominant phase.

To further analysis the structure of BTFW, a refinement had been carried out using XRD data. All the reflection peaks of the X-ray profiles were indexed. The unit cell and fitting parameters of the sample are computed and given in table 1. The refinement results show that the chemical composition deviated from the nominal one and a few of oxygen vacancies appeared, which was ascribed to the appearance of a small quantity of $BaWO_4$, which presents the secondary phase in the BTFW sample.

It is interesting to find out the regularities governing the formation of pervoskite-type compounds and use them to further guide the exploration of new materials. It is well known that in early 1920s, Goldschmidt [18] has proposed a tolerance factor '$t$' to study the stability of pervoskites, defined as:

$$t = (r_{\mathrm{A}} + r_{\mathrm{O}})/\sqrt{2}(r_{\mathrm{B}} + r_{\mathrm{O}}), \tag{3}$$

**Table 1.** Refined structural parameters for $BaTi_{0.5}Fe_{0.33}W_{0,17}O_3$ after the Rietveld refinements of X-ray diffraction data.

| $BaTi_{0.5}Fe_{0.33}W_{0,17}O_3$ | Hexagonal | Cubic double |
|---|---|---|
| Space group | $P6_3/mmc$ | Fm m |
| Cell parameters | $a = b = 5.758$ (1) Å<br>$c = 14.073$ (7) Å | $a = b = c = 8.032$ (1) Å |
| Cell volume | 404.113 (2) Å$^3$ | 518.239 (4) Å$^3$ |
| Discrepancy factors (%) | $R_{wp} = 10.1$<br>$R_p = 5.83$<br>$R_F = 3.10$<br>$\chi^2 = 4.22$ | |
| Bragg *R*-factor | 2.75 | 3.65 |
| | Angular positions and intensities of the most intense peaks of two phases | |
| $2\theta(^\circ)$ | 31.02 | 31.47 |
| Intensity (a.u.) | 17542 | 5530 |

where $r_A$, $r_B$ and $r_O$ are ionic radii of A-site cation, B-site cation and oxygen, respectively. Tolerance factor is a geometry describing the mismatch of A- and B-site ions in the compound, as was demonstrated by Hwang *et al* [19] and Teresa *et al* [20]. The tolerance factor was first suggested by Megaw [21] to determine the stability of the pervoskite phase for a given set of anions and cations. In general, when the value of '*t*' nears 1, the pervoskite phase will be formed in the cubic structure [22]. For $t > 1.06$, a hexagonal structure is expected, which is classified by the stacking sequence of the $BO_6$ octahedra [23]. However, recently the works of Jiang *et al* [24], Moreira and Dias [25] and Ubic [26] offered more precise, albeit empirical, estimation of pervoskite cell parameters based on ionic radii. In light of these facts and taking into account the values of ionic radii of different atoms [27], the tolerance factor value ($t = 1.063$) has been estimated and it is within the range of stable pervoskite structure. We also note that '*t*' is greater than 1.06, which is in agreement with the results of the refinement.

Figure 2c shows the typical microstructure of BTFW ceramic. The round- and plate-like grains are the two typical grain morphologies in this ceramic. This type of microstructure was typical for this type of derivative $BaTiO_3$ (doped or undoped hexagonal barium titanate ceramics 'h-$BaTiO_3$') [28]. It is interesting that the grain morphologies were consistent with the crystal structures.

XRD can be utilized to evaluate peak broadening with crystallite size, and lattice strain due to dislocation. The crystallite size of BTFW was determined by the X-ray line broadening method using the Scherrer formula, Williamson–Hall technique (W–H) and SEM. The Sherrer formula can be written as [29]:

$$D = \frac{K\lambda}{\beta_{Sch}\cos(\theta)}, \tag{4}$$

where $D$ is the crystallite size in nanometres, $\lambda$ the X-ray wavelength (1.54056 Å for $CuK_\alpha$ radiation), $K$ a constant equal to 0.9, $\theta$ the Bragg angle of the most intense peak and $\beta_{Sch}$ the line broadening at FWHM on the highest peak of planes (220) and (110), which is located at about $2\theta = 31^\circ$. The broadening of diffraction lines occurs for two principal reasons: instrumental effects and physical origins [30]. To decouple these contributions, it is necessary to collect a diffraction pattern from the line broadening of a standard material such as silicon to determine the instrumental broadening [31]. The instrument-corrected broadening is defined as:

$$\beta_{Sch} = \sqrt{\beta^2_{observed} - \beta^2_{instrumental}}, \tag{5}$$

where, $\beta_{observed}$ is the measured broadening and $\beta_{instrumental}$ the instrumental broadening of the diffraction peak from a standard silicon sample.

The presence of micro-distortions induces both isotropic and anisotropic broadening of the Bragg reflections. The micro-distortions are local variations of the reticular distances, produced by non-uniform crystalline distortions. They are generated by crystalline defects, such as stacking faults, vacancies or insertions, as well as by local variations of the chemical composition. A simple way to understand this effect is to consider that the presence of micro-distortions is equivalent to the existence of micro-strain, which involves a distribution of the reticular distance variables. In Williamson–Hall method [32], strain induced broadening arising from crystal imperfection and distortions were related by:

$$\beta_s = 4\varepsilon\tan(\theta). \tag{6}$$

Here $\varepsilon$ is the root mean square value of the micro-strain $\varepsilon = \Delta d/d$. Assuming that the particle size and strain contributions to line broadening are independent of each other and both have a Cauchy-like profile, the observed line breadth is simply the sum of the two:

$$\beta_{hkl} = \beta_{Sch} + \beta_s = \frac{k\lambda}{D\cos(\theta)} + 4\varepsilon\tan(\theta) \tag{7}$$

which means:

$$\beta_{hkl}\cos(\theta) = \frac{k\lambda}{D} + 4\varepsilon\sin(\theta). \tag{8}$$

A plot is drawn with $\sin(\theta)$ along the $x$-axis and $\beta_{hkl}\cos(\theta)$ along the $y$-axis for as-prepared and annealed BTFW ceramic (figure 2a and b). In view of that, the slope and $y$-intersect of the fitted line represent the strain and the particle size, respectively. We can say that the calculated crystallite size using W–H technique is larger than that obtained by using Scherrer's technique, but lies well in the range with less size distribution (see table 2). This may be due to the presence of strain, which contributes also to the broadening of peaks. A negative strain for samples may be attributed to the lattice shrinkage. The grain sizes observed by SEM are larger than those calculated by the Scherrer and W–H techniques. This can be explained by the fact that each particle observed by SEM is formed by several grains crystallized.

### 3.2 *Optical study*

Spectroscopic ellipsometry (SE) is a non-destructive optical technique that allows the study of complex optical properties of materials. Optical properties of BTFW compound have been investigated using ellipsometry measurements. In the ellipsometry experiments, the change of an incident polarized light after reflection from the surface of a sample is measured and analysed. Two parameters of $\psi$ and $\Delta$, which represent respectively the amplitude ratio and phase shift of the parallel and perpendicular components of the reflected light, are measured in the experiments. These are related to the optical and structural properties of the samples and defined by [33]

$$\rho = \tan(\psi)\exp(i\Delta). \tag{9}$$

**Table 2.** Calculated grain sizes, crystallite sizes and strains of hexagonal and cubic double phases of $BaTi_{0.5}Fe_{0.33}W_{0,17}O_3$ (H-BTFW and C-BTFW).

| Average size and strain | H-BTFW | C-BTFW |
|---|---|---|
| $D_{SEM}$ (nm) | ∼2000 | ∼400 |
| $D_{sch}$ (nm) | 55 | 34 |
| $D_{W-H}$ (nm) | 57 | 37 |
| $\varepsilon$ | −0.00113 | 0.00234 |

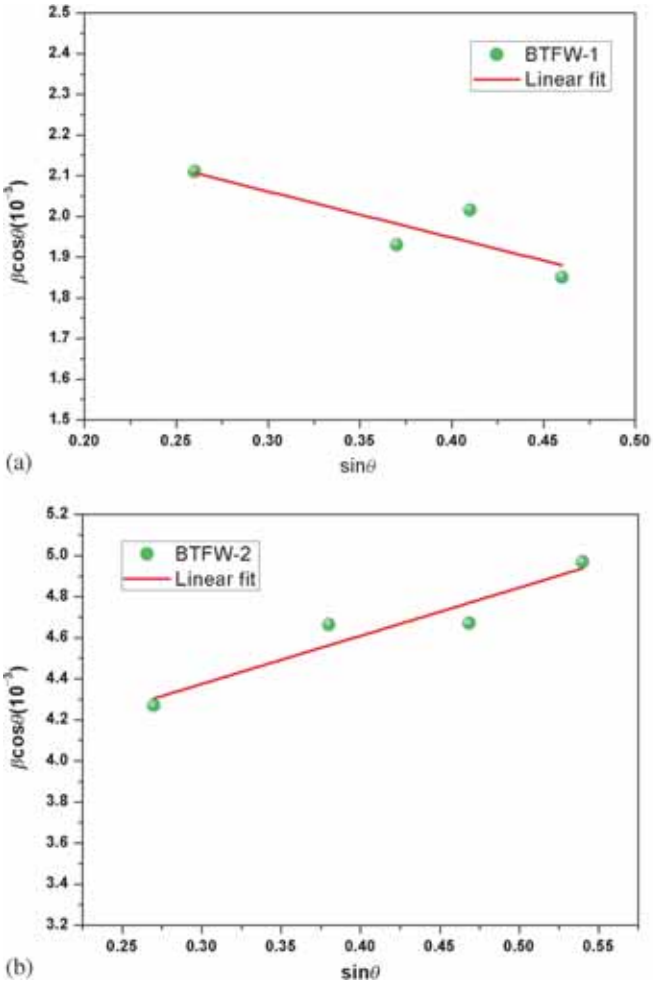


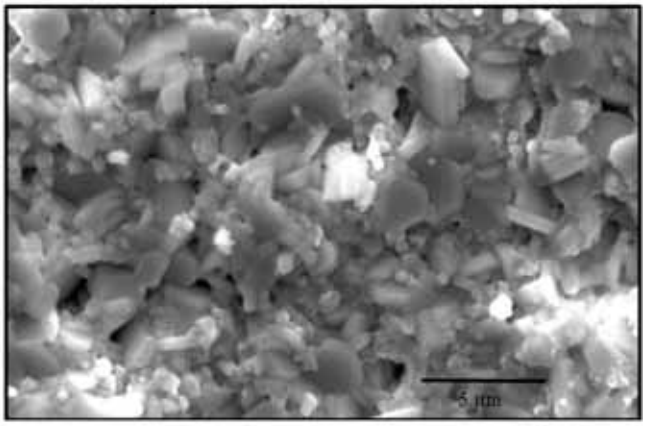


**Figure 2.** Strain graphs of the (**a**) hexagonal phase, (**b**) cubic double phase and (**c**) the SEM image of $BaTi_{0.5}Fe_{0.33}W_{0,17}O_3$ ceramic sintered at 1400°C.

The complex dielectric function ($\varepsilon^*$) of this ceramic is a common representation via the two-phase (air/simple) model [34]:

$$\varepsilon^* = \varepsilon_1 + i\varepsilon_2 = \sin^2(\phi)\left[1 + \left(\frac{1-\rho}{1+\rho}\right)\tan^2(\phi)\right]. \quad (10)$$

The complex dielectric function is obtained from the $\psi$ and $\Delta$ values and given by [35]

$$\varepsilon^* = \varepsilon_1 + i\varepsilon_2 = (n^*)^2 = (n + ik)^2. \quad (11)$$

From which the following arise:

$$\begin{cases} \varepsilon_1 = n^2 - k^2 & (12) \\ \varepsilon_2 = 2nk & (13) \end{cases}$$

where $n$ and $k$ are refractive index and extinction coefficient, respectively.

The plots of evaluated real and imaginary dielectric functions ($\varepsilon_1, \varepsilon_2$) for the sample in 1.40–4.96 (eV) range are shown in figure 3. The imaginary part of the dielectric function presents a monotonic variation (strictly increasing), which does not like the real part behavior which shows, at the beginning, an increase. Then, an important decrease is clearly observed, because there is a relation between dielectric function ($\varepsilon_1, \varepsilon_2$) and optical constant ($n, k$):

$$n = \frac{1}{\sqrt{2}}\sqrt{\sqrt{\varepsilon_1^2 + \varepsilon_2^2} + \varepsilon_1} \quad (14)$$

$$k = \frac{1}{\sqrt{2}}\sqrt{\sqrt{\varepsilon_1^2 + \varepsilon_2^2} - \varepsilon_1}. \quad (15)$$

The optical constant of BTFW ceramic compound can be derived from the data of dielectric function. Figure 4 shows the photon energy dependences of refractive index $n$ and extinction coefficient $k$ of BTFW in the photon energy range of 1.40–4.96 (eV). From figure 4, we find that the optical constant spectra of BTFW shows a low refractive index ($n$ = 1.38–1.61) in the UV–visible region. In the beginning, the $n$-values increase. Then, they decrease when the photon energy increases from 1.4 to 4.96 eV. The refractive index for this sample shows a peak around 3.75 eV (330 nm) and subsequently decreases slowly showing dispersion with photon energy. The peak in the refractive index indicates the onset of the absorption. The $k$-values of BTFW increase when photon energy increases, which is in accordance with Kramers–Kronig relations. In addition, the values of extinction coefficients are low at lower photon energy, which indicates that the absorption loss is low in the higher wavelength range studied here. The $n$-values can reflect the degree of crystalline quality of BTFW ceramic. The gradual increase in the $n$-values means that the crystalline quality of this compound is increased, which is in accordance with the XRD measurements. At the wavelength of 600 nm (2.06 eV), the refractive index is 1.42, which is less than many other traditional compounds of $BaTiO_3$ with different methods of preparation [36–41]. The electrical insulator materials with low refractive index and low absorption are needed for various optical devices, such as low loss waveguides, resonators, photonic crystals, distributed Bragg reflectors, light-emitting diodes, passive splitters, biosensors, attenuators and filters [42–44]. These low values of $n$ may be caused by the existence interstice coming from a few of oxygen vaccines. It is well known that the refractive index is affected by crystallinity, electronic band structure and lattice point defects [45]. The basic $BO_6$ octahedral building block in perovskite ferroelectrics leads to similarities in band structure and similarities in polarization-induced, stark-like energy band shifts. The B-cation, d-orbital and the O-anion 2p orbital associated with each octahedron are the major contributors to refractive indices.

The principal methods of determining the electron band structures of materials are optical methods. The relation between attenuation coefficient (absorption coefficient) and the extinction coefficient is given by

$$k = \frac{\alpha\lambda}{4\pi}. \quad (16)$$

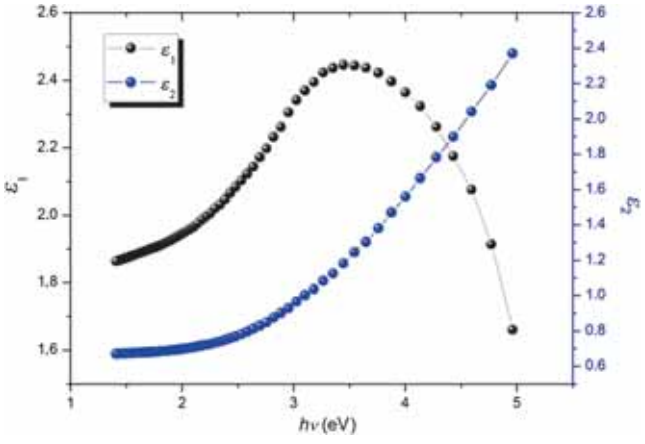


**Figure 3.** Real and imaginary part of dielectric function of BTFW ceramic.

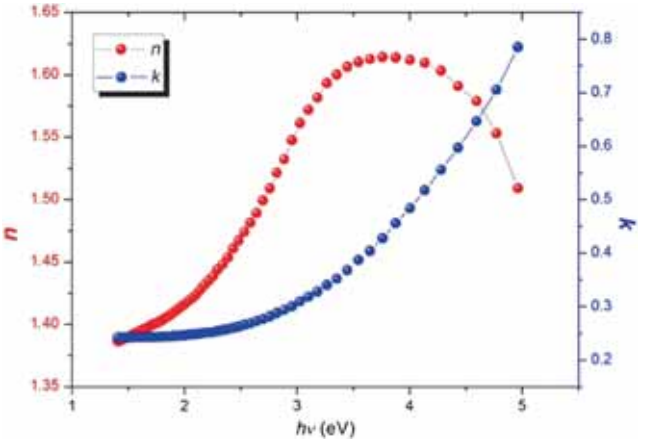


**Figure 4.** Optical constants ($n$ and $k$) of BTFW ceramic.

If there is no light absorption in media, it can be seen that $k = \alpha = 0$.

It is known that in the absorption process, a photon of known energy excites an electron from lower to a higher energy state, corresponding to an absorption edge. In crystalline materials, the fundamental edge is directly related to the conduction and valence band; that is, direct and indirect bandgaps. The dependence of absorption coefficient on photon energy in the high absorption regions is carried out to obtain the detailed information about the energy bandgaps. The relation between absorption coefficient and the incident photon energy is given by Davis and Mott [46] by the following relation:

$$\alpha(\upsilon) = B\frac{(h\upsilon - E_g^{opt})^m}{h\upsilon}, \tag{17}$$

where $B$ is a constant related to the extent of the band tailing, $E_g^{opt}$ the optical bandgap, $h\upsilon$ the incident photon energy and $m$ the index which have different values 2, 3, 0.5 and 0.33 corresponding to indirect allowed, indirect forbidden, direct allowed and direct forbidden transitions, respectively [47]. Figure 5 shows the absorption coefficients $\alpha$ as a function of the incident energy for BTFW pervoskite. From figure 5, we observe that the absorption coefficients increase quickly with increase in photon energy. It clearly shows that the absorption edge was obtained for the higher energy. It can be observed that $\alpha$ for BTFW is about $5 \times 10^4$ cm$^{-1}$ at $\sim$2 eV, increases rapidly with the incident energy and is above $40 \times 10^5$ cm$^{-1}$ at 5 eV. The high value around the fundamental absorption edge reflects the good quality of the sample used in the present work. The optical bandgap energy for BTFW ceramic has been estimated by using the equation of a direct bandgap semiconductor near the band edge, for photon energy $h\upsilon$ greater than the optical bandgap energy, $E_g^{opt}$, of the semiconductors, i.e.,

$$\alpha h\upsilon = B(h\upsilon - E_g^{opt})^{0.5}. \tag{18}$$

The plots of $(\alpha h\upsilon)^2$ *vs.* energy $h\upsilon$ (known as Tauc plots) for BTFW ceramic is shown in figure 6. The bandgap energy is obtained by extrapolating the linear part of the Tauc plots to the energy axis (i.e., where $(\alpha h\upsilon)^2 = 0$). The calculated direct optical bandgap energy is 4.36 eV; this means that the absorption edge is 284 nm. This value of direct optical bandgap is very close to that obtained in $BaTiO_3$ (4.37 eV) prepared by the sol–gel method and sintered at 600°C [48]. Gaur and Sharma [48] reported that the optical bandgap calculated through UV–visible spectrophotometer varies from 4.37 to 3.80 eV for their samples sintered at 600 to 1000°C, respectively. Thomas *et al* [49] reported that the bandgap energy of $BaTiO_3$ films is 3.75 eV, and the bandgap energy decreases with the increase in annealing temperature. Tian *et al* [50] reported that the bandgap energies of $Ba_{0.9}Sr_{0.1}TiO_3$ thin film are 4.33 eV for 500°C, 4.14 eV for 600°C and 4.11 eV for 730°C, and the composition-dependent optical bandgap was investigated by increasing the Ba/Sr ratio from 0.7 to 1.0, as a result of which the bandgap decreased from 4.15 to 3.75 eV [50]. It is noted that these reported values of the $BaTiO_3$ depend on the elaboration method and doped element affecting the oxygen octahedron. In the studied chemical composition, $Ba^{2+}$ (1.61 Å) ion enter the A-site of $ABO_3$ pervoskite structure, whereas $Ti^{4+}$ (0.60 Å), $Fe^{3+}$ (0.64 Å) and $W^{6+}$ (0.6 Å) ions occupy the B-site. For $ABO_3$ pervoskite, the $BO_6$ octahedron governs the low-lying conduction band (CD) and the valence band (VB) maximum [51]. Dopants in B-site lead to distortion of oxygen-octahedral structure. The relatively larger ionic radius of the B ion enhances the thermal stability of the $BO_6$ octahedra [52]. So the orbital hybridization between O 2p and B-site d will be weakened and the energy bandgap is widened to some degree and vice versa.

The impurity and unit cell distortion causes defect in the band, which raises the intermediary levels within the bandgap region. The width of defect bands formed in the

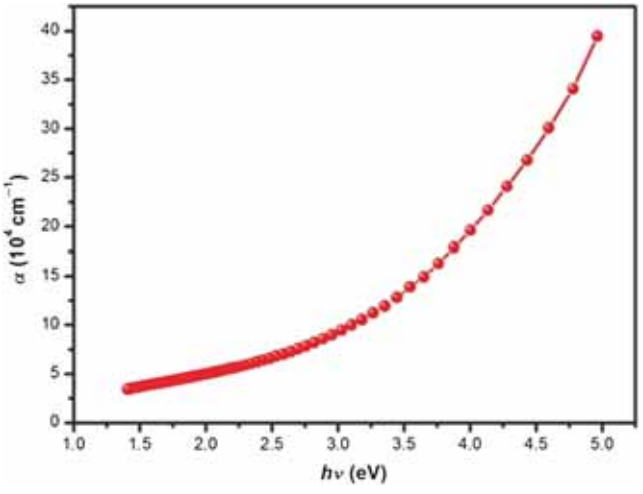


**Figure 5.** Optical absorption coefficient $\alpha$ of BTFW ceramic.

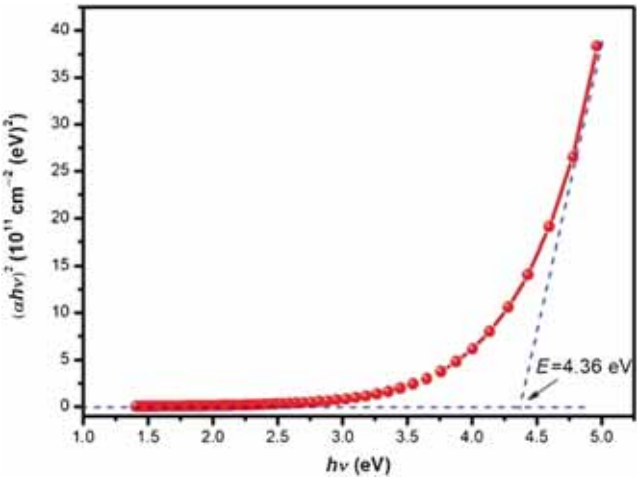


**Figure 6.** Plot of $(\alpha h\upsilon)^2$ *vs.* $h\upsilon$ for BTFW, the optical bandgap energy $E_g$ is deduced from extrapolation of the straight line to $(\alpha h\upsilon)^2 = 0$.

bandgap is associated with Urbach tail [53]. The equation of Urbach energy is given by [53,54]

$$\alpha = \alpha_0 \exp(h\nu/E_U). \tag{19}$$

This relation can be rewritten as

$$\mathrm{Ln}(\alpha) = \frac{h\nu}{E_U} + \alpha_0'', \tag{20}$$

where $\alpha_0''$ is a constant and $E_U$ the Urbach energy, which indicates the width of the band tails of the localized states and is used to characterize the degree of disorder in amorphous and crystalline solids. By plotting the $\mathrm{Ln}(\alpha)$ as a function of $h\nu$, as it is shown in figure 7, the values of $E_U$ and $\alpha_0''$ can be calculated and is equal to 1.42 eV and 9.2 $\mathrm{cm}^{-1}$, respectively. The existence of the extended band and the localized states may be mainly associated with the structural disorder produced by mixture of cubic double and hexagonal pervoskite phases, impurities, defects, grain boundaries and dangling bond states in BTFW ceramic.

In the context of the determination of the energy that characterizes our sample, we also investigated the photon energy dependence of refractive index using Wemple and DiDomenico single-effective-oscillator model which relates the $n$ and $h\nu$ in the below bandgap region by [55]:

$$n^2(h\nu) = 1 + \frac{E_{SO}E_d}{E_{SO}^2 - (h\nu)^2}. \tag{21}$$

Where $E_{SO}$ (SO = single oscillator energy) is the average excitation energy for electronic transitions and is empirically related to the optical bandgap, while $E_d$ is the dispersion energy and is a measure of the average strength of inter-band optical transitions and can be considered as a parameter having very close relation with the charge distribution within a unit cell and therefore with the chemical bonding [56,57]. The dependence of $(n^2–1)^{-1}$ on the square of photon energy $(h\nu)^2$ for BTFW is shown in figure 8. The values of $E_{SO}$ and $E_d$ were deduced from the intercept determined from the extrapolation of the line to $(n^2–1)^{-1}$ axis and the slope. Values of $E_{SO}$ and $E_d$ are 15.40 and 23.18 eV, respectively.

The dispersion energy $E_d$ is a measure of the strength of interband optical transitions and can be considered as a parameter having very close relation with the charge distribution within unit cell and therefore with the chemical bonding. This parameter is given by

$$E_d = \beta N_c Z_a N_e, \tag{22}$$

where $N_c$ is the nearest-neighbour cation coordination number, $Z_a$ the formal anion valency, $N_e$ the effective number of valence electrons per anion and $\beta$ a constant whose value depends on the chemical bonding character of material. For our sample, $N_c = 6$, $Z_a = 2$ and $N_e = 8$. It was declared that the constant $\beta$ can assume two values: $\beta_i = 0.26 \pm 0.04$ eV for ionic compounds and $\beta_c = 0.39 \pm 0.05$ eV for covalent compounds [55,58]. Just like halides and most oxides, $\beta$ takes on the ionic value ($\beta = 0.24$ eV). Based on the single-oscillator model, the single-oscillator parameters $E_{SO}$ and $E_d$ are connected to the imaginary part $\varepsilon_2$ of the complex dielectric constant and the $-1$ and $-3$ moments of the $\varepsilon_2$ optical spectrum can be derived from the following relations [59]:

$$E_{SO}^2 = \frac{M_{-1}}{M_{-3}} \quad \text{and} \quad E_d^2 = \frac{M_{-1}^3}{M_{-3}}. \tag{23}$$

The calculated values of $M_{-1}$ and $M_{-3}$ moments are determined as 1.22 (dimensionless) and 0.07 $(\mathrm{eV})^{-2}$, respectively. It is known that the static dielectric constant substance is defined as:

$$\varepsilon_r(0) = \lim_{\nu \to 0}(n^2(h\nu)) = n_0^2 = 1 + \frac{E_d}{E_{SO}}. \tag{24}$$

So, the knowledge of dispersion parameters allows us to determine the static dielectric constant of materials. The zero-frequency refractive index ($n_0$) and dielectric constant ($\varepsilon_0$) were calculated as $n(0) = 1.58$ and $\varepsilon(0) = 2.5$.

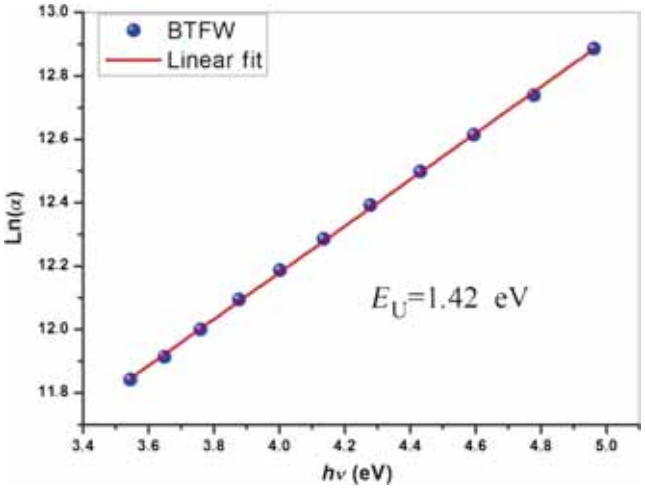


**Figure 7.** The logarithmic plots of the absorption coefficient as a function of incident photon energy near the absorption edge region.

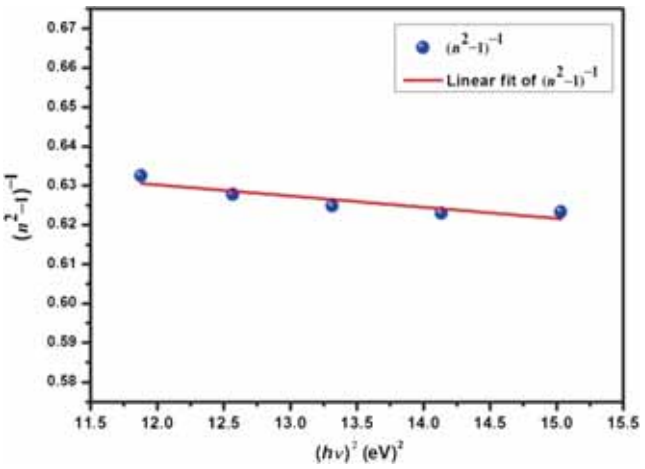


**Figure 8.** Linear fitting curves of $(n^2–1)^{-1}$ dependent on $(h\nu)^2$ for BTFW ceramic.

In physics, the dissipation factor tan($\delta$) is a measure of loss-rate of power of a mechanical mode, such as oscillation, in a dissipative system. For example, electric power is lost in all dielectric materials, usually in the form of heat. The dissipation factor tan($\delta$) can be calculate according to the following equation [60]:

$$\tan(\delta) = \frac{\varepsilon_2}{\varepsilon_1}. \tag{25}$$

The variation of tan($\delta$) for the investigated ceramic with $h\nu$ is shown in figure 9. It is found that the dissipation factor increases with increase in the photon energy.

Optical conductivity $\sigma_{\text{opt}}$ is one of the important quantities that describes the optical properties of materials. $\sigma_{\text{opt}}$ is used to detect the allowed interband optical transitions of a material. The complex optical conductivity ($\sigma^*$) is related to the complex dielectric constant ($\varepsilon^*$) by the following relation [61]:

$$\sigma_1 = \omega\varepsilon_2\varepsilon_0 \quad \text{and} \quad \sigma_2 = \omega\varepsilon_1\varepsilon_0, \tag{26}$$

where $\omega$ is the angular frequency and $\varepsilon_0$ the free space dielectric constant. The real and imaginary parts of the optical conductivity dependence of frequency are shown in figure 10. It is seen in this figure that the real part increases with increasing frequency, while the imaginary part increases to an energy (exactly equal to the optical bandgap found by the method of Davis and Mott in figure 6, $h\nu = 4.36$ eV $= E_g^{\text{opt}}$) then decreases.

From the values of $\varepsilon_1$ and $\varepsilon_2$ we obtained the complex electric modulus and the complex impedance ($M^*$ and $Z^*$), which is given as follows [62]:

$$M^* = \frac{1}{\varepsilon^*} = M_1 + jM_2 = \frac{\varepsilon_1}{(\varepsilon_1^2 + \varepsilon_2^2)} + j\frac{\varepsilon_2}{(\varepsilon_1^2 + \varepsilon_2^2)} \tag{27}$$

$$Z^* = \frac{1}{j\omega C_0 \varepsilon^*} = \frac{M^*}{j\omega C_0} = Z_1 + jZ_2, \quad j^2 = -1, \tag{28}$$

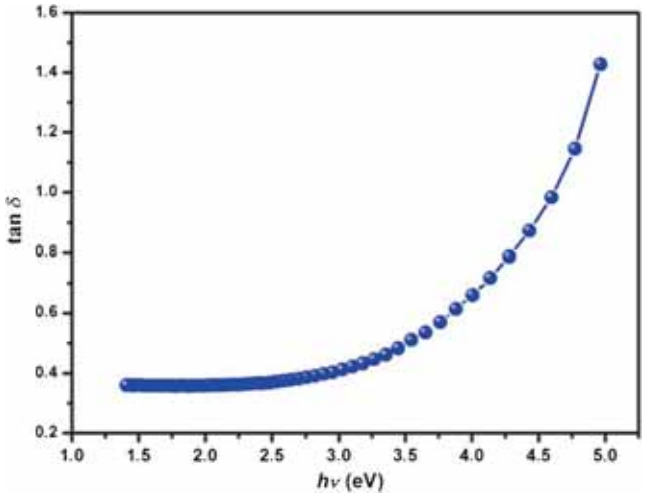


**Figure 9.** Spectral dependence of the loss factor (tan $\delta$) for BTFW ceramic.

where $M_1$ and $M_2$ are the real and imaginary parts of the electric modulus, respectively, $Z_1$ and $Z_2$ are the real and imaginary parts of the complex impedance, respectively, and $C_0 = (A/e)\varepsilon_0$ is the vacuum capacitance of the cell, where

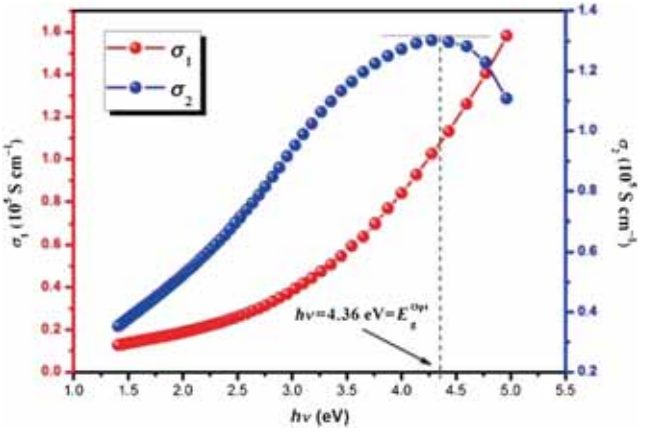


**Figure 10.** Spectral dependence of the real and imaginary parts of optical conductivity of the BTFW compound.

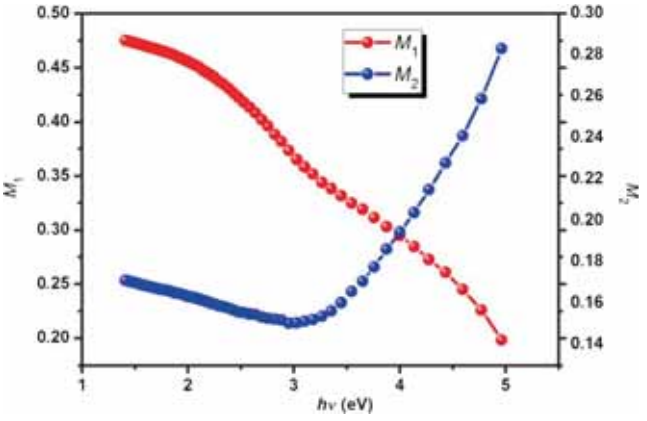


**Figure 11.** Variation of $M_1$ and $M_2$ as a function of photon energy for the BTFW ceramic.

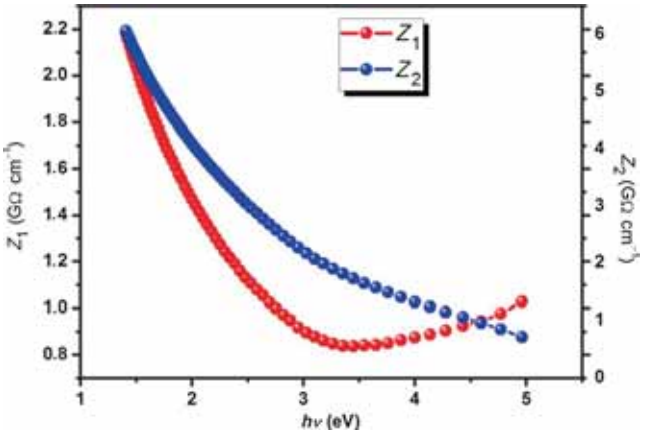


**Figure 12.** Variation of $Z_1$ and $Z_2$ as a function of photon energy for the BTFW ceramic.

$\varepsilon_0$ is the free space dielectric constant, $A$ and $e$ are the area and the thickness of ceramic BTFW, respectively. The variation of $M_1$ and $M_2$ for the investigated ceramic with $h\nu$ is shown in figure 11. Also, the complex electric modulus is a powerful parameter to acquire information about the relaxation mechanism [63]. Figure 12 shows the variation of the real and imaginary part of the impedance as a function of energy photon.

## 4. Conclusion

The material $BaTi_{0.5}(Fe_{0.33}W_{0.17})O_3$ was prepared by a solid-state reaction method. Structural and optical properties of this ceramic compound have been studied. Rietveld analysis of XRD data shows the mixture phases (cubic double and hexagonal) of crystal structure at room temperature, and the particle sizes observed by SEM are larger than those calculated by XRD, which indicates that each particle observed by SEM consists of many crystallized grains. The optical properties of BTFW have been investigated by SE. The refractive index of the BTFW increases and then decreases when the photon energy increases. The extinction coefficient also increases when photon energy increases. The optical absorption coefficient $\alpha$ of BFTW, which is calculated from the ellipsometric data, has shown a high value around the fundamental absorption edge and reflects the good quality of our sample. The direct optical bandgap energy was estimated to be ∼4.36 eV, which is in good agreement with those reported by other authors. It is understood that the difference of the bandgap energy is mainly because of the distortion of oxygen-octahedral structure. The optical dispersion parameters existed by the single-oscillator model of Wemple–DiDomenico, when the single-oscillator energy ($E_{SO}$) and the dispersion energy ($E_d$) are 15.40 and 23.18 eV, respectively. The zero-frequency refractive index as well as the dissipation factor ($\tan(\delta)$), the optical conductivity ($\sigma_{opt}$), the complex electric modulus ($M^*$) and the complex impedance ($Z^*$) of this ceramic were calculated optically. This opens the door to control the structural and the optical properties of pervoskite materials and leads to important industrial applications such as: solar cells, electronic and optoelectronic devices with a low price.

## References


[1] Sasirekha N, Rajesh B and Chen Y-W 2008 *Indian Chem. Res.* **47** 1868

[2] Zhu W, Akbar S A, Asiaie R and Dutta P K 1997 *J. Appl. Phys.* **36** 214

[3] Yogo T, Yamamoto T, Sakamoto W and Hirano S 2004 *J. Mater. Res.* **19** 3290

[4] Hu M Z C, Miller G A, Payzant E A and Rawn C J 2007 *J. Mater. Sci.* **35** 2927

[5] Choi G J, Lee S K, Woo K J, Koo K K and Cho Y S 1998 *Chem. Mater.* **10** 4104

[6] Huybrechts B, Ishizaki K and Takata M 1995 *J. Mater. Sci.* **30** 2463

[7] Wang X S, Zhang L L, Liu H, Zhai J W and Yao X 2008 *Mater. Chem. Phys.* **112** 675

[8] Nedelcu L *et al* 2013 *Appl. Surf. Sci.* **278** 158

[9] Devi S and Jha A K 2009 *Asian J. Chem.* **21** 117

[10] Devi S and Jha A K 2009 *Phys. B* **404** 4290

[11] Lin F and Shi W 2010 *J. Alloys Comp.* **495** 167

[12] Ivanov S A, Eriksson S G, Erikssen J, Tellgren R and Rundlof H 2004 *Mater. Res. Bull.* **39** 615

[13] Grey I E, Li C, Cranswick L M D, Roth R S and Vanderah T A 1998 *J. Solid State Chem.* **135** 312

[14] Dang N V, Nguyen H M, Chuang P Y, Thanh T D, Lam V D, Lee C H and Hong L V 2012 *Chinese J. Phys.* **50** 262

[15] Rietveld H M 1969 *J. Appl. Crystallogr.* **2** 65

[16] Aspnes D E 2014 *Thin Solid Films* **571** 334

[17] Zidi N, Chaouchi A, d'Astorg S, Rguiti M and Courtois C 2014 *J. Alloys Comp.* **590** 557

[18] Goldschmidt V M 1958 *Geochemistry* (London: Oxford University Press)

[19] Hwang H Y, Choeng S W, Radaelli R G, Marezio M and Batlog B 1995 *Phys. Rev. Lett.* **75** 914

[20] de Teresa J M, Ibarra M R, Garcia J, Blasco J, Ritter C, Algarabel P A, Marguina C and del Moral A 1996 *Phys. Rev. Lett.* **6** 3392

[21] Megaw H D 1946 *Proc. Phys. Soc.* **58** 133

[22] Reaney I M and Ubic R 1999 *Ferroelectric* **228** 23

[23] Shikano M, Ishiyama O, Inaguma Y, Nakamura T and Itoh M 1995 *J. Solid State Chem.* **120** 238

[24] Jiang L Q *et al* 2006 *J. Phys. Conf. Series* **67** 1531

[25] Moreira R L and Dias A 2007 *J. Phys. Conf. Series* **68** 1617

[26] Ubic R 2007 *J. Am. Ceram. Soc.* **90** 3326

[27] Shannon R D 1976 *Acta Crystallogr. A* **32** 751

[28] Zhao F, Yue Z, Pei J, Zhuang H, Gui Z and Li L 2007 *J. Am. Ceram. Soc.* **90** 2461

[29] Taylor A 1961 *X-ray metallography* (New York: Wiley)

[30] Mittemeijer E J and Scardi P 2004 *Diffraction analysis of the microstructure of materials* (Berlin: Springer)

[31] Biju V, Sugathan N, Vrinda V and Salini S L 2008 *J. Mater. Sci.* **43** 1175

[32] Wiliamson G K and Hall W H 1953 *Acta Metall.* **1** 22

[33] Jellison G E and Modine F A 1996 *Appl. Phys. Lett.* **69** 371

[34] Loyalka S K and Riggs C A 1995 *Appl. Spectroscopy* **49** 1107

[35] Marfing J 1980 *J. Physique* **41** 971

[36] Car dona M 1965 *Phys. Rev.* **140** 651

[37] Pasierb P, Komornicki S and Radecka M 1998 *Thin Solid Films* **324** 134

[38] Thomas R, Dube D C, Kamalasanan M N and Chandra S 1999 *Thin Solid Films* **346** 212

[39] Pencheva T and Nenkov M 1998 *Thin Solid Films* **324** 305

[40] Lee M K, Liao H C, Tung K W, Shih C M and Shih T H 2002 *J. Phys. D: Appl. Phys.* **35** 61

[41] Tanga X G, Chana H L W and Dingb A L 2004 *Thin Solid Films* **460** 227

[42] Zhou H, Kim H K, Shi F G, Zhao B and Yota J 2002 *Microelectron. J.* **33** 999

[43] Xi J Q, Kim J K and Schubert E F 2005 *Nano Lett.* **5** 1385

[44] Memisevic J, Korampally V, Gangopadhyay S and Grant S A 2009 *Sens. Actuators A* **141** 227

[45] Wanga H, Xua J, Maa C, Zhaoa P, Wanga L, Biana L, Rena W and Changa A 2015 *Ceram. Inter.* **41** 475

[46] Mott N F and Davis E A 1979 *Electronic processes in non-crystalline materials* (Oxford: Clarendon Press)

[47] Ming Oo H, Mohamed-Kamari H and Wan-Yusoff W M D 2012 *Int. J. Mol. Sci.* **13** 4623

[48] Gaur A and Sharma N 2013 *World Acad. Sci. Eng. Technol.* **7** 1209

[49] Thomas R, Dube D C, Kamalasanan M N and Chandra S 1999 *Thin Solid Films* **346** 212

[50] Tian H Y, Luo W G, Pu X H, He X Y, Qiu P S, Ding A L, Yang S H and Mo D 2001 *J. Phys.: Condens. Matter.* **13** 4065

[51] Duan Z H, Hu Z G, Jiang K, Li Y W, Wang G S, Dong X L and Chu J H 2013 *Appl. Phys. Lett.* **102** 151908

[52] Wu L, Wei C, Wu T and Liu H 1983 *J. Phys. C: Solid State Phys.* **16** 2803

[53] Pant M, Kanchant D K and Condaliya N 2009 *Mater. Chem. Phys.* **115** 98

[54] Urbach F 1953 *Phys. Rev.* **92** 1324

[55] Wemple S H and DiDomenico M 1971 *Phys. Rev. B* **3** 1338

[56] Meng L J and Dos Santos M P 1993 *Thin Solid Films* **226** 22

[57] Meng L J, Andritschky M and Dos Santos M P 1993 *Thin Solid Films* **223** 242

[58] Wemple S H and DiDomenico M 1970 *Phys. Rev. B* **1** 193

[59] Salem A M 2002 *Appl. Phys. A* **74** 205

[60] Fadel M, Fayek S A, Abou-Helal M O, Ibrahim M M and Shakra A M 2009 *J. Alloys Compd.* **485** 604

[61] Yakuphanoglu F, Sekerci M and Ozturk O F 2004 *Opt. Commun.* **239** 275

[62] Dash S, Choudhary R N P and Kumar A 2014 *J. Phys. Chem. Solids* **75** 7713

[63] Sharma S, Shamim K, Ranjana A, Raib R, Kumarib P and Sinha S 2015 *Ceram. Inter.* **41** 7713